Supporting information for

Photo-transformation of nitrate and fulvic acid driven by guest iron minerals

Na Huang[a,1], Yuanyuan Chen[a,1], Xuyin Yuan[a], Yingying Li[a], Yin Lu[a], Yilan Jiang[a], Huacheng Xu[b], Lingxiao Ren[c], Dawei Wang[a,*]

a Key Laboratory of Integrated Regulation and Resource Development of Shallow Lakes, Ministry of Education, College of Environment, Hohai University, Nanjing 210098, P.R. China

b State Key Laboratory of Lake Science and Environment, Nanjing Institute of Geography and Limnology, Chinese Academy of Sciences, Nanjing 210008, China

c School of Environmental Engineering, Nanjing Institute of Technology, Nanjing 210008, China

Dawei Wang

Phone: +86 13245803369

E-mail: dawei.wang@hhu.edu.cn

[1] These authors contributed equally to this work.

Number of pages: 28

Number of Texts: 5

Number of Figures: 15

Number of Tables: 4

Text S1. Detection methods for nitrogen species and total organic carbon.

The concentrations of nitrate (NO_3^-), nitrite (NO_2^-), and ammonia (NH_4^+) in the solution were detected according to appropriate colorimetric methods. NO_3^- was quantified using ultraviolet (UV) spectrophotometry following national standard HJ/T246-2007 at wavelengths λ=220 nm and λ=275 nm. NO_2^- was measured using N-(1-naphthyl)-ethylenediamine spectrophotometry as per the national standard GB7493-87 at a wavelength of λ = 540 nm (Meng et al., 2022).The standard indophenol blue reagent colorimetric method was adopted to analyze the concentration of NH_4^+ at a wavelength of λ = 625 nm in the solution (Jiang et al., 2022; Shi et al., 2022)**.** Total nitrogen (TN) was measured by alkaline potassium persulfate digestion UV spectrophotometric method (HJ 636-2012), and total organic carbon (TOC, TShimadzu, TOC-L CPH, Japan) was tested to analyze the mineralization of fulvic acid (FA).

Text S2. Characterization of *α*-Fe_2O_3.

The crystal structure of *α*-Fe_2O_3 was detected by X-ray diffraction (XRD, Ultima IV, Japan). The microstructure of *α*-Fe_2O_3 was characterized by High-resolution transmission electron microscopy (HR-TEM, FEI Tecnai F20, USA). The UV–vis diffuse reflectance spectrums (DRS) were tested on the Soildspec-3700 spectrometer to characterize the light absorption ability of *α*-Fe_2O_3. Then X-ray photoelectron spectroscopy (XPS, Thermo ESCALAB 250 Xi, USA) technology was employed to analyze the surface chemical states of Fe 2p for *α*-Fe_2O_3.

Text S3. Quantification of hydroxyl radical.

Hydroxyl radical (•OH) quantification was conducted according to a previous study (Pan et al., 2023). Excessive TPA (5 mmol/L) was used as a chemical probe to react with •OH to generate hTPA. The hTPA concentration is analyzed by a fluorescence detector (FLD) (Ex=313 nm, Em= 300 ~ 500 nm). The hTPA standard curve is shown in Fig. S1.

Text S4. Fluorescence excitation-emission matrix regional integration.

The DOMFluor toolbox (https://doi.org/10.4319/lom.2008.6.572b) was used to standardize three-dimensional excitation-emission matrix fluorescence spectroscopy (3D-EEM). Briefly, the 3D-EEM data were preprocessed using Matlab code to subtract the spectral values measured on the Milli-Q ultrapure water blank from the test spectra of the experimental samples. Raman and Rayleigh scatter bands (first and second order) were trimmed in each EEM. Corrected EEMs were normalized by their intensities, along with using non-negative constraints (Bro, 1997; Du et al., 2023). The 3D-EEM spectrums are divided into five regions, labeled as I, II, III, IV, and V. The self-built code is used to sample and integrate the different regions of the EEM spectrums (He et al., 2024).

Text S5. Fourier transform ion cyclotron resonance mass spectrometer coupled with electrospray ionization data acquisition and processing.

The main detection parameters are: The injection method is continuous injection, the injection speed is 120 μL/h, the capillary inlet voltage is 4.0 kV, the ion accumulation time is 0.2 s, and the collection mass range is 100 ~ 800 Da, the number of sampling points is 4 M 32-bit data, and the time domain signal is superimposed 300 times to improve the signal-to-noise ratio. Before sample detection, the instrument was calibrated with 10 mmol/L sodium formate. After sample detection, soluble organic matter (known molecular formula) was used for internal standard calibration. After correction, the mass errors detected were less than 1 mg/L. Molecular formula matching: The mass spectrum data is calibrated with the internal standard using known CHO compounds in NOM. After calibration, the molecular formula is matched according to the following parameters; S/N>4, the range of the number of elements is as follows, the range of the number of elements is as follows, C1-∝H1 -∝, O1-∝, N0-3, S0-1, get possible molecular formula results. Molecular formula screening: retain molecular formulas with 0.2<=H/C<=2.2 and 0<=O/C<=1.2; retain molecular formulas with the averages of double-bond equivalents (DBE_w) values in the range of -10 ~ 10; if an m/z value corresponds to multiple possible molecular formulas, it is correct to retain the smallest molecular formula with the number of heteroatoms (N+S number sum). If there are still non-unique molecular formulas, it is correct to retain the molecular formula with the smallest error value. Based on the elemental ratios of O/C and H/C, all compounds detected were classified into several major biochemical classes (Xu et al., 2018). Substances not within the following ranges were not analyzed in detail.

1: Lipids H/C = 1.5 ~ 2.0, O/C = 0 ~ 0.3;

2: Aliphatic/proteins H/C = 1.5 ~ 2.2, O/C = 0.3 ~ 0.67;

3: Carbohydrates H/C =1.5 ~ 2.4, O/C = 0.67 ~ 1.2;

4: Unsaturated hydrocarbons H/C = 0.7 ~ 1.5, O/C = 0 ~ 0.1;

5: Lignins/CRAM-like structures H/C = 0.7 ~ 1.5, O/C = 0.1 ~ 0.67;

6: Tannin H/C = 0.6 ~ 1.5, O/C = 0.67 ~ 1.0;

7: Aromatic structures H/C = 0.2 ~ 0.7, O/C = 0 ~ 0.67.

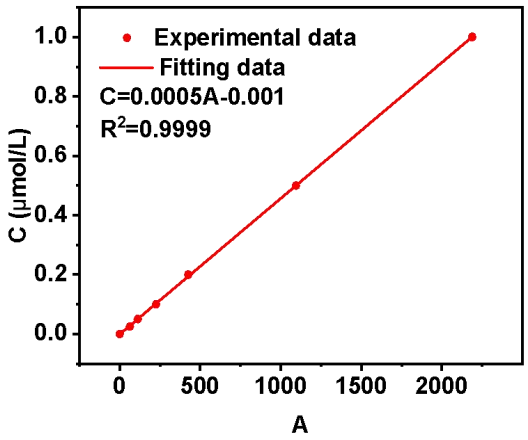

Fig. S1. The linear standard curve of hTPA concentration and fluorescence intensity.

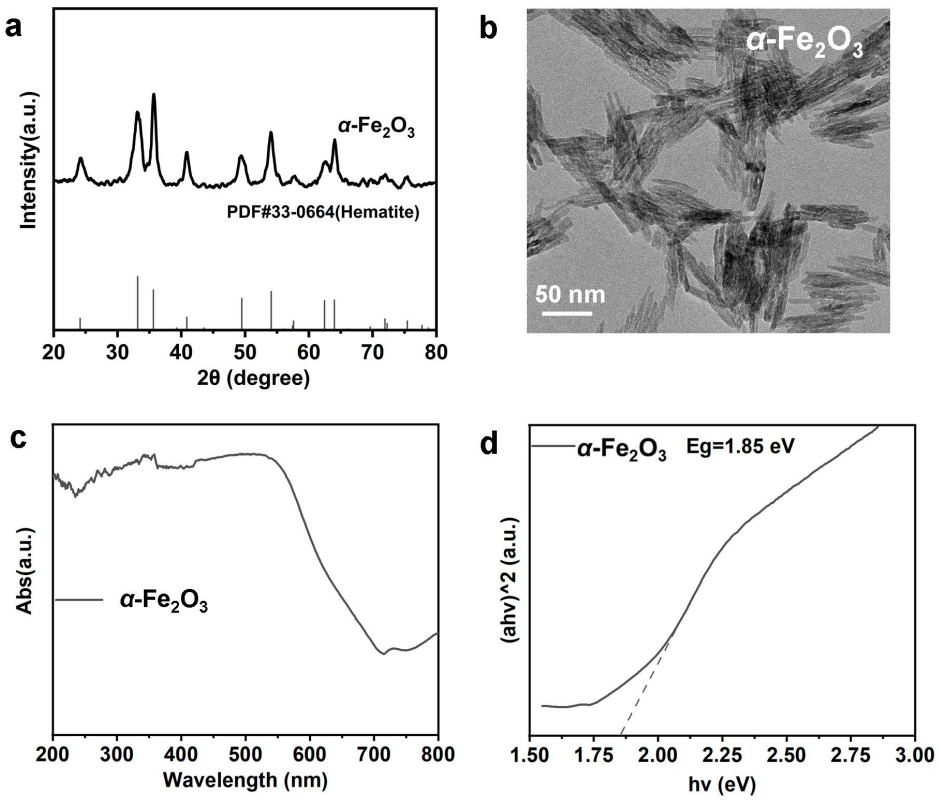

Fig. S2. (a) XRD pattern; (b) HR-TEM images; (c) UV-vis DRS and (d) Band gap Tauc's diagrams of α-Fe_2O_3.

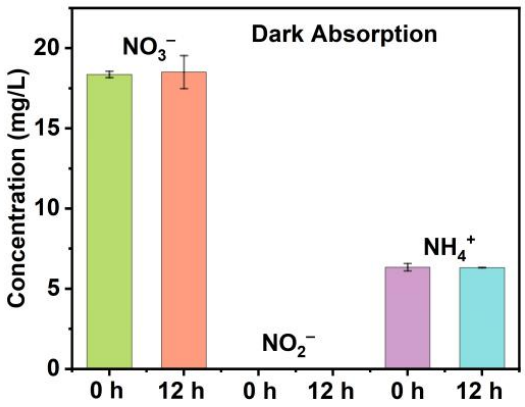

Fig. S3. Adsorption performance of α-Fe_2O_3 on NO_3^- and FA under dark conditions. Experimental conditions: $c_0(NO_3^-)$ = 20 mg-N/L, c_0(FA) = 100 mg-C/L, α-Fe_2O_3 dosage = 0.4 g/L.

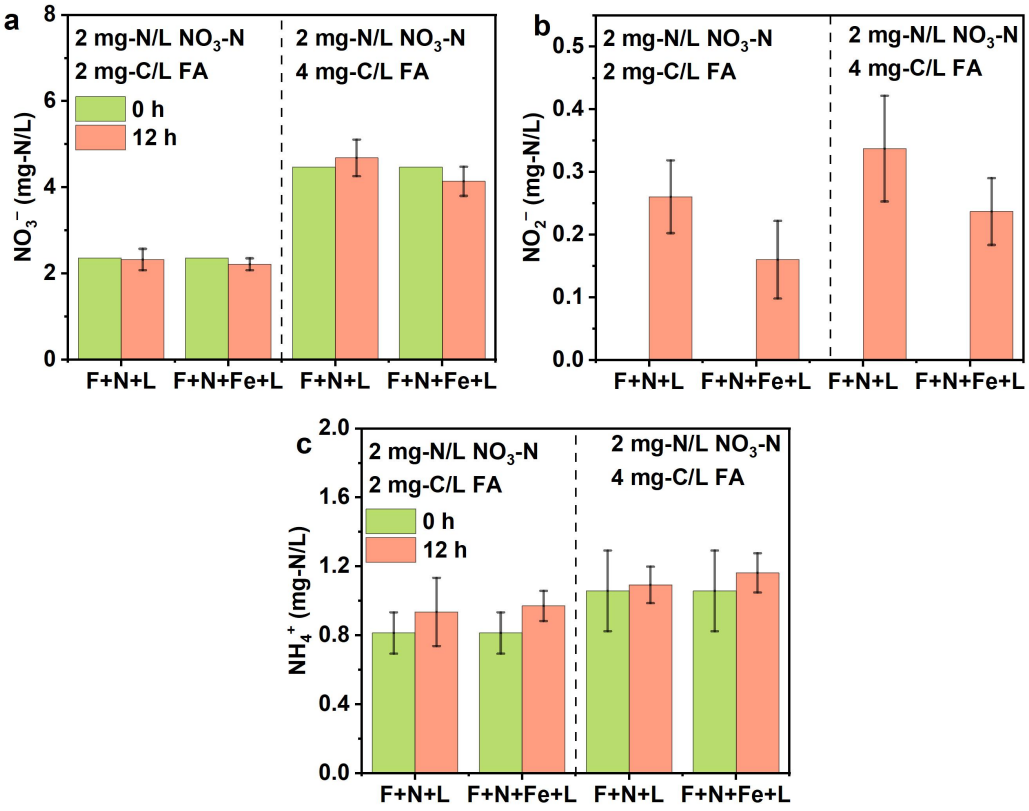

Fig. S4. Transformation of nitrogen species at low concentrations (a) NO_3^-, (b) NO_2^-, and (c) NH_4^+. Experimental conditions: $c_0(NO_3^-)$ = 2 mg-N/L, c_0(FA) = 2 or 4 mg-C/L, α-Fe_2O_3 dosage = 0.4 g/L. (N, F, Fe, and L are the abbreviations of NO_3^-, FA, α-Fe_2O_3, and UV_{254} irradiation, respectively).

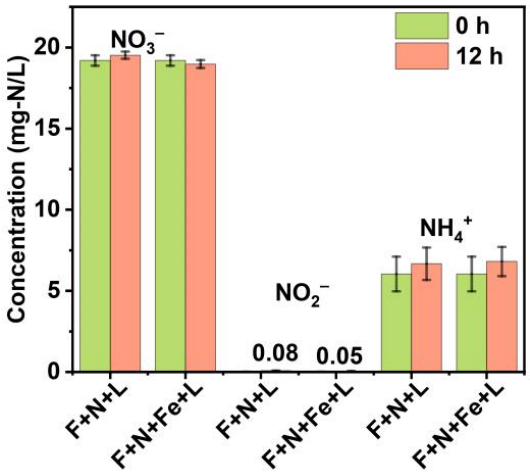

Fig. S5. Changes in nitrogen species concentration under the xenon lamp irradiation. Experimental conditions: $c_0(NO_3^-)$ = 20 mg-N/L, c_0(FA) = 100 mg-C/L, α-Fe_2O_3 dosage = 0.4 g/L. (N, F, Fe, and L are the abbreviations of NO_3^-, FA, α-Fe_2O_3, and xenon lamp irradiation, respectively).

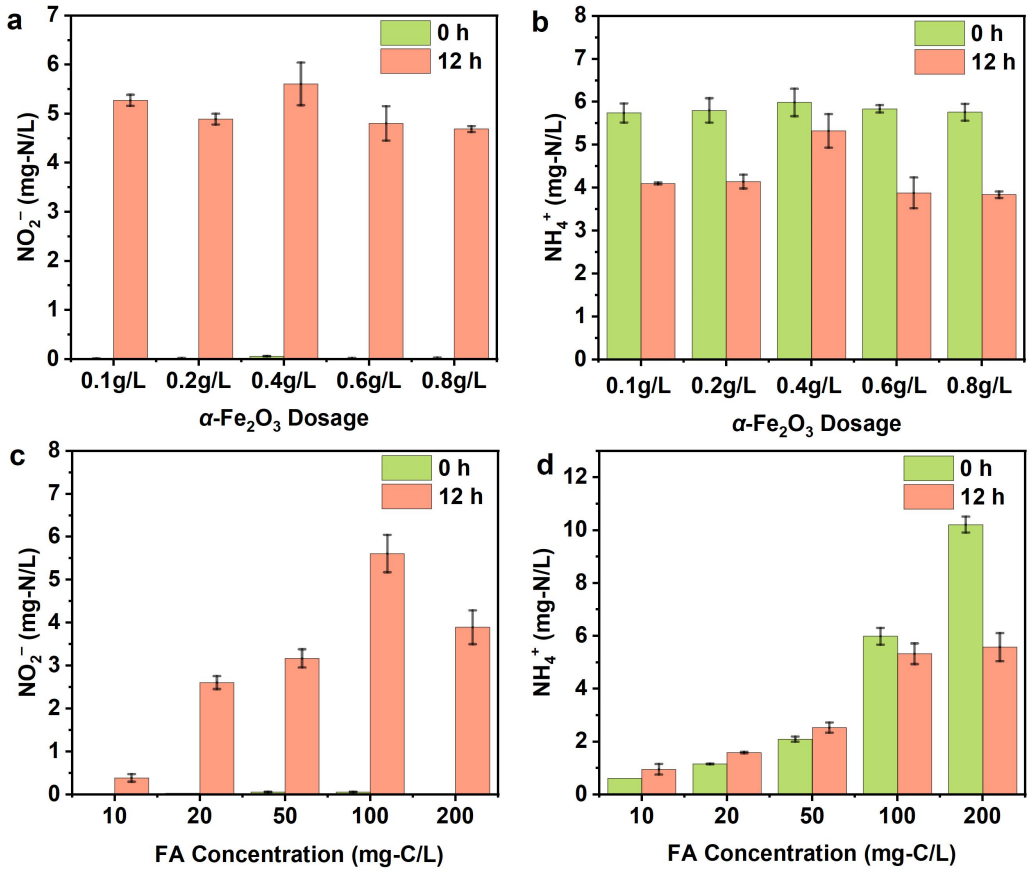

Fig. S6. Effect of (a and b) α-Fe_2O_3 dosage and (c and d) FA concentration on the NO_3^- photochemical products by α-Fe_2O_3. Experimental conditions: $c_0(NO_3^-)$ = 20 mg-N/L, c_0(FA) = 10 ~ 100 mg-C/L, α-Fe_2O_3 dosage = 0.1 ~ 0.4 g/L. (N, F, Fe, and L are the abbreviations of NO_3^-, FA, α-Fe_2O_3, and UV_{254} irradiation, respectively).

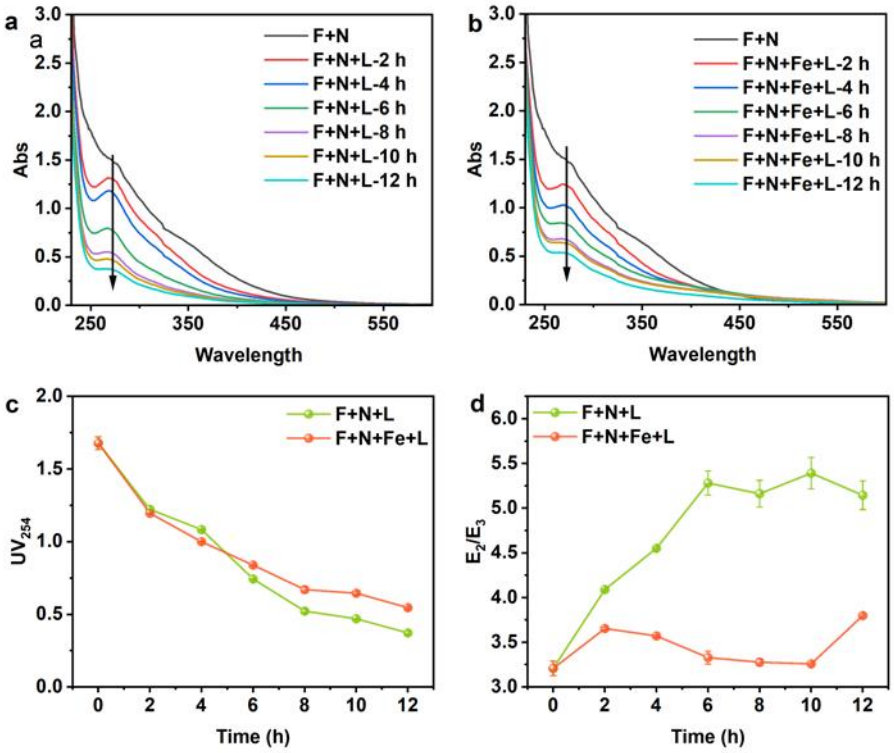

Fig. S7. UV absorbance of (a) F+N+L and (b) F+N+Fe+L. The changes of (c) UV_{254}, and (d) E_2/E_3 with the incubation time in the F+N+L and F+N+Fe+L systems.

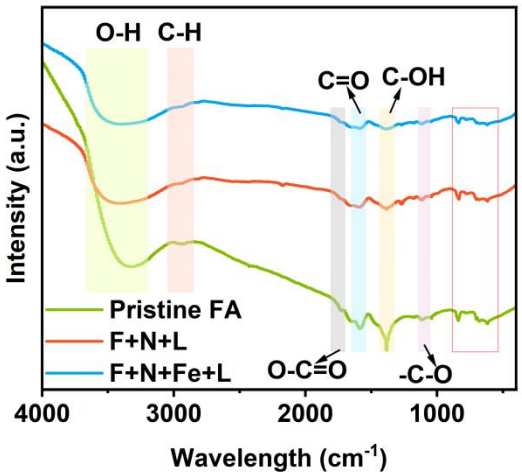

Fig. S8. Variation of FTIR spectra of FA in the F+N+L and F+N+Fe+L systems.

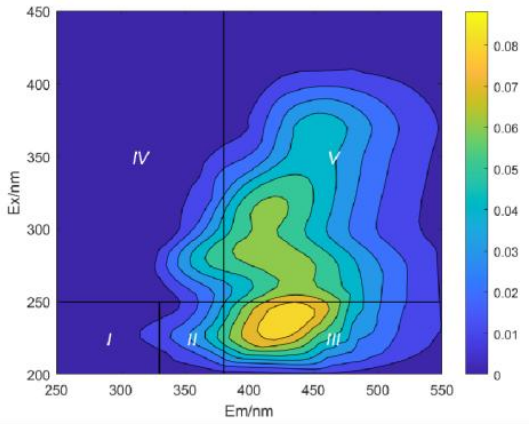

Fig. S9. 3D-EEM of pristine FA. Regions I and II are related to simple aromatic proteins, and regions III−V represent fulvic acid, soluble microbial by-products-like, and humic acid-like substances respectively (Chen et al., 2003).

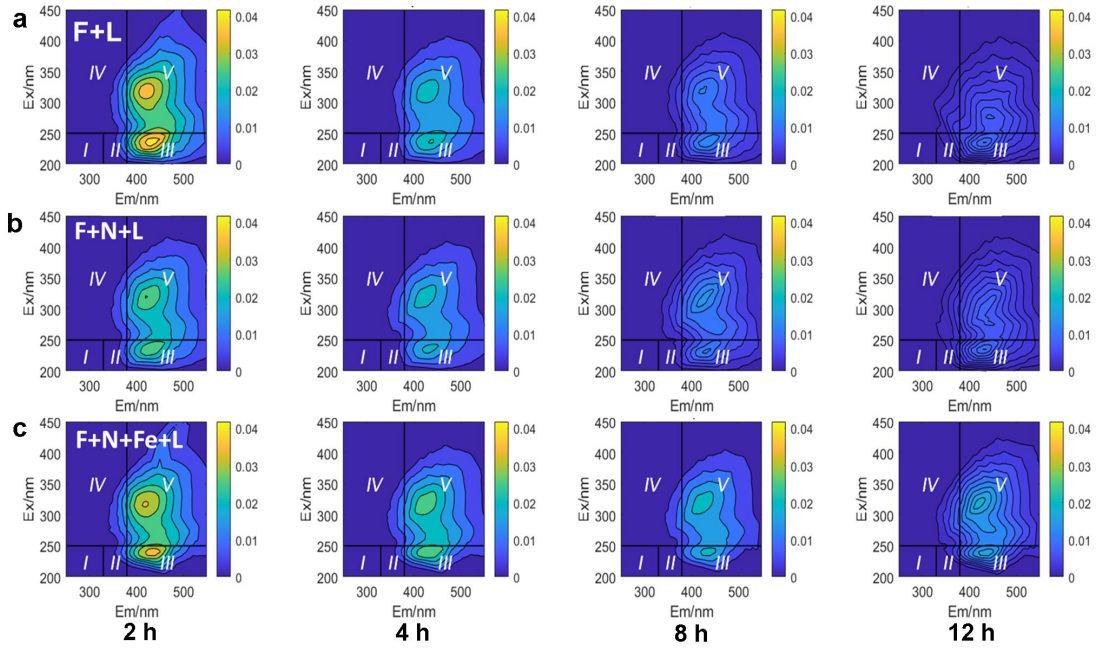

Fig. S10. Variation in fluorescence intensity of FA photochemical products of 3D-EEM spectra with radiation time in the different systems: (a) F+L, (b) F+N+L, (c) F+N+Fe+L. Horizontal and vertical lines divide the 3D-EEM into five regions (I−V).

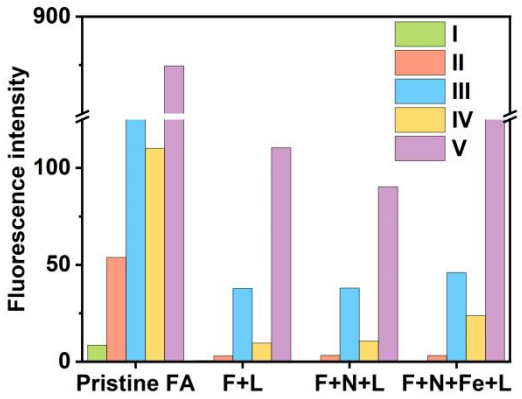

Fig. S11. Regional fluorescence intensity of the initial FA and photochemical reaction products after 12 h. Regions I and II are related to simple aromatic proteins, regions III−V represent fulvic acid, soluble microbial by-products-like, and humic acid-like substances respectively (Chen et al., 2003).

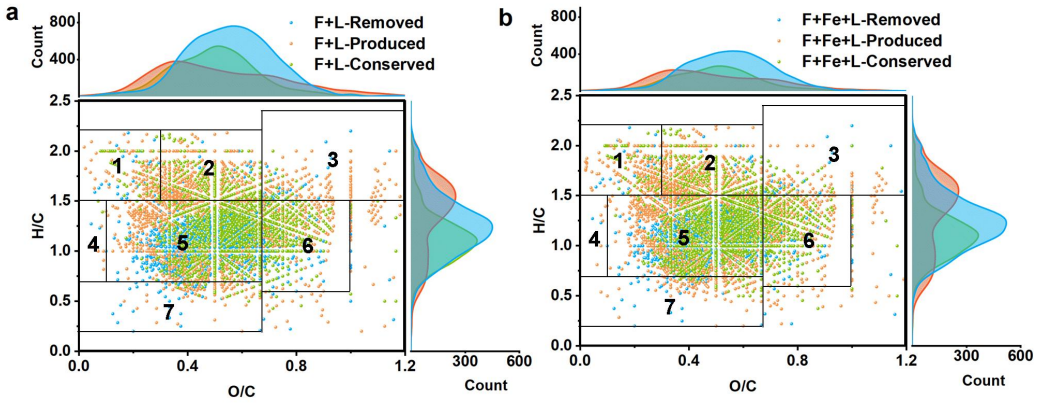

Fig. S12. The Van Krevelen diagrams of composition variation in FA (a) F+L and (b) F+Fe+L. (1: Lipids; 2: Aliphatic/Proteins, 3: Carbohydrates; 4: Unsaturated hydrocarbons; 5: Lignins/CRAM-like structures; 6: Tannin; 7: Aromatic structures.)

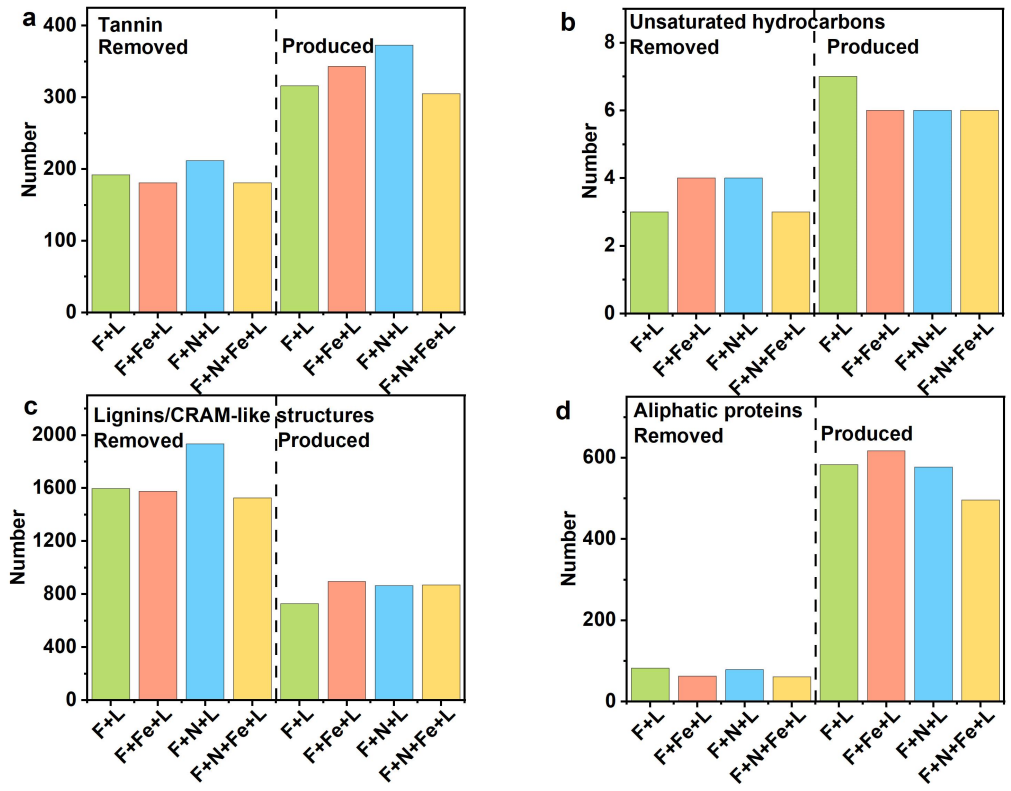

Fig. S13. Number of molecules of removed and produced by (a) Tannin, (b) unsaturated hydrocarbons, (c) lignins/CRAM-like structure, and (d) aliphatic proteins compounds.

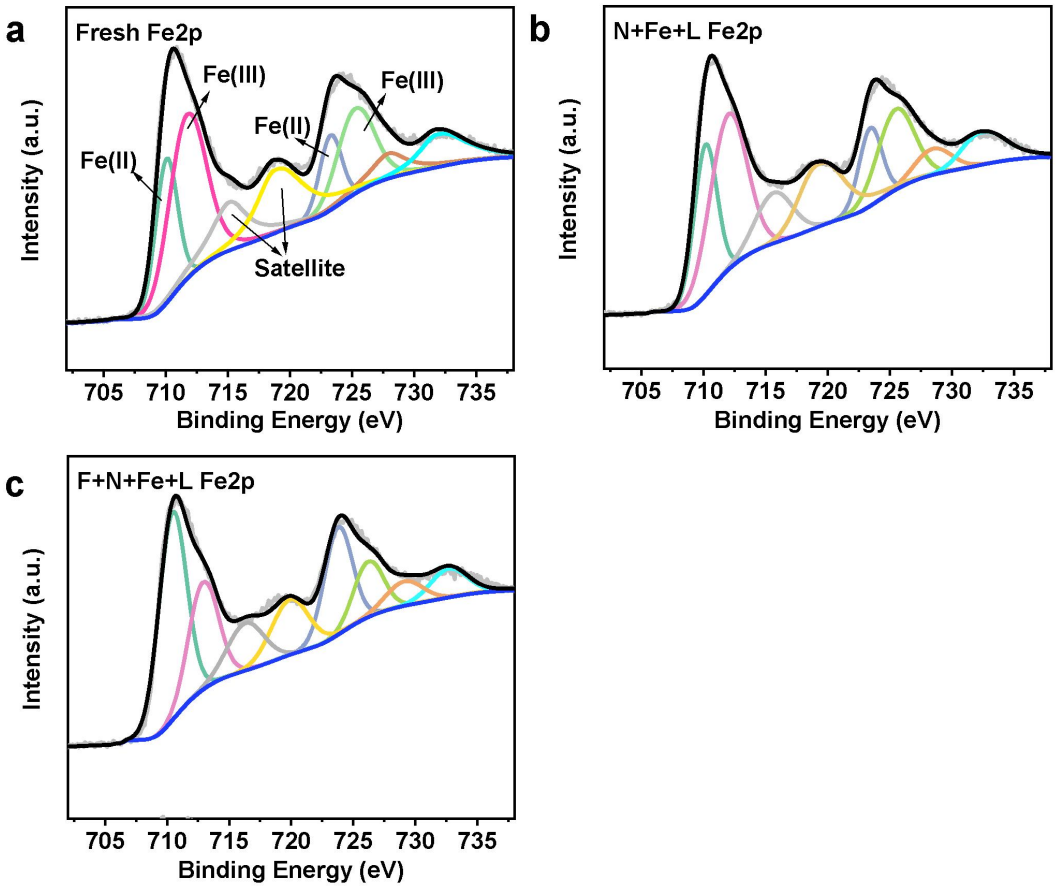

Fig. S14. XPS Fe 2p spectra for (a) pristine α-Fe_2O_3, and α-Fe_2O_3 subject to reactions in (b) N+Fe+L, and (c) F+N+Fe+L systems after 12 h of irradiation.

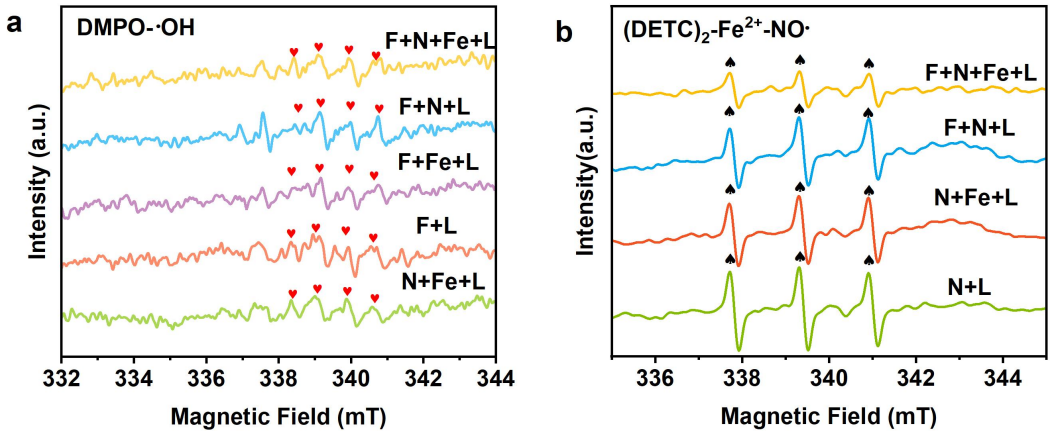

Fig. S15. Spin-trapping ESR spectra for (a) DMPO- •OH and (b) $(DETC)_2$-Fe^{2+}-NO• in different systems.

Table S1. Summary of the possible photochemistry reactions of FA (He et al., 2024; Li et al., 2023).

Mass difference	Formula difference	Transformation reaction
		Dealkyl group
–14.02665	(-CH_2)	Demethylation
–28.0533	(-C_2H_4)	Deethylation
–42.07995	(-C_3H_6)	Deisopropyl
–26.03765	(-C_2H_2)	Dealkylation
		Oxygen addition
47.9847438	(+3O)	Tri-hydroxylation
34.0054792	(+H_2O_2)	Di-hydroxylation
31.9898292	(+2O)	Di-hydroxylation
29.9741792	(-H_2+O_2)	Methyl to carboxylic acid
18.0105646	(+H_2O)	hydrogenation+ hydroxylation
15.9949146	(+O)	Hydroxylation
13.9792646	(-H_2+O)	Alcohol to carboxylic acid
		Reaction of carboxylic acid
–28.0059146	(-CO)	Loss of CO
–30.0215646	(-CH_2O)	Loss of formaldehyde
–44.0008292	(-CO_2)	Decarboxylation
		Reaction of amine
0.9840426	(-NH_2+ OH)	Oxidative displacement of amine
1.0316074	(-NH_3+O)	Deamination to ketone
–15.010872	(-NH)	Deamination
–17.026522	(-NH_3)	Ammonia elimination
–25.006222	(-CONH+ H_2O)	Hydrolysis of amide
		Reaction of the sulfate
15.9771561	(-SH+OH)	Oxidative displacement of sulfhydryl
–31.9720707	(-S)	Desulfurization
–63.9618999	(-SO_2)	Desulfonation
–79.9568145	(-SO_3)	Desulfonation
		Other reaction
2.01565	(+H_2)	Hydrogenation
1.9682646	(-CH_2+O)	Oxidative methyl to alcohol

Table S2. Water quality parameters of the natural water from Xuanwu Lake.

	Concentration
pH	7.32
COD (mg/L)	6.00
BOD_5 (mg/L)	1.20
NO_3^- (mg-N/L)	1.20
NO_2^- (mg-N/L)	Not detected
NH_4^+ (mg-N/L)	0.32
TN (mg/L)	2.36
TP (mg/L)	0.18
TOC (mg-C/L)	6.10

Table S3. The number of possible precursor-product pairs represents the relationships between the molecules removed and produced.

Formula difference	F+L	F+Fe+L	F+N+L	F+N+Fe+L
Dealkyl group				
($-CH_2$)	121	152	115	158
($-C_2H_4$)	113	171	141	141
($-C_3H_6$)	147	166	171	177
($-C_2H_2$)	148	172	168	166
Oxygen addition				
(+3O)	103	114	114	130
($+H_2O_2$)	155	138	159	138
(+2O)	134	114	136	134
($-H_2+O_2$)	109	118	115	131
($+H_2O$)	163	162	156	160
(+O)	130	133	121	138
($-H_2+O$)	117	134	124	134
Reaction of carboxylic acid				
(-CO)	140	136	122	151
($-CH_2O$)	128	149	136	148
($-CO_2$)	121	109	119	134
Reaction of amine				
($-NH_2$+ OH)	96	106	99	111
($-NH_3$+O)	108	98	82	95
(-NH)	109	127	127	131
($-NH_3$)	132	130	111	113
(-CONH+ H_2O)	125	100	116	137
Reaction of the sulfate				
(-SH+OH)	69	77	88	173
(-S)	79	81	91	155
($-SO_2$)	41	47	44	89
($-SO_3$)	43	51	53	84
Other reactions				
($+H_2$)	151	138	131	146
($-CH_2+O$)	114	154	155	158

Table S4. XPS analysis of α-Fe_2O_3 before and after different treatments.

	Fe(II)	Fe(III)
Fresh α-Fe_2O_3	33.9%	66.1%
N+Fe+L	50.3%	49.7%
F+N+Fe+L	65.5%	34.5%

References

Bro, R. (1997). PARAFAC. Tutorial and applications. Chemometrics and intelligent laboratory systems 38(2): 149-171.

Chen, W., Westerhoff, P., Leenheer, J.A. and Booksh, K (2003). Fluorescence excitation− emission matrix regional integration to quantify spectra for dissolved organic matter. Environmental Science & Technology, 37(24): 5701-5710.

Du, P., Chen, G., Zhang, P., Yang, B. and Wang, J (2023). Photo-transformation of wastewater effluent organic matter reduces the formation potential and toxicity of chlorinated disinfection byproducts. Ecotoxicology and Environmental Safety, 265: 115515.

He, H., Sun, N., Li, L., Zhou, H., Hu, A., Yang, X., Ai, J., Jiao, R., Yang, X., Wang, D. and Zhang, W (2024). Photochemical Transformation of Dissolved Organic Matter in Surface Water Augmented the Formation of Disinfection Byproducts. Environmental Science & Technology, 58 (7): 3399–3411

Jiang, C., Zhang, M., Dong, G., Wei, T., Feng, J., Ren, Y. and Luan, T (2022). Photocatalytic nitrate reduction by a non-metal catalyst h-BN: Performance and mechanism. Chemical Engineering Journal 429: 132216.

Li, X., Shen, J., Cao, H., Zhang, W., Sun, Z., Ma, F. and Gu, Q (2023). Molecular transformation of dissolved organic matter during persulfate-based advanced oxidation: Response of reaction pathways to structure. Chemical Engineering Journal, 474: 146256.

Meng, N., Ma, X., Wang, C., Wang, Y., Yang, R., Shao, J., Huang, Y., Xu, Y., Zhang, B. and Yu, Y (2022). Oxide-derived core–shell Cu@ Zn nanowires for urea electrosynthesis from carbon dioxide and nitrate in water. ACS nano, 16(6): 9095-9104.

Pan, Y., Zheng, X., Zhao, G., Rao, Z., Yu, W., Chen, B. and Chu, C (2023). Water Vapor Condensation on Iron

Minerals Spontaneously Produces Hydroxyl Radical. Environmental Science & Technology, 57(23): 8610-8616.

Shi, H., Li, C., Wang, L., Wang, W., Bian, J. and Meng, X (2022). Photocatalytic reduction of nitrate pollutants by novel Z-scheme ZnSe/$BiVO_4$ heterostructures with high N_2 selectivity. Separation and Purification Technology, 300:121854.

Xu, H., Li, Y., Ding, M., Chen, W., Wang, K. and Lu, C (2018). Simultaneous removal of dissolved organic matter and nitrate from sewage treatment plant effluents using photocatalytic membranes. Water Research, 143: 250-259.